Heat transfer enhancement in dense suspensions of agitated solids. Part II: Experiments in the exchange limit

Xinglong Chen, Michel Louge *

Sibley School of Mechanical and Aerospace Engineering, Cornell University, Ithaca, NY 14853, USA

ABSTRACT

We test the theory of Part I in the exchange limit by vibrating acrylic and aluminum spheres in a box consisting of two flat, vertical isothermal walls, two bumpy, horizontal, insulated walls, and two flat vertical insulated surfaces. The steady heat flux through the thermally-guarded hot wall is recorded at different temperatures of the opposite wall cooled by thermoelectric modules, and enhancements of suspension conductivity are calculated using a lumped-parameter model of the box. To compare results and theory, we also predict vertical profiles of agitation and solid volume fraction in the box using granular dynamics.

© 2008 Elsevier Ltd. All rights reserved.

1. Introduction

The heat transfer to dense suspensions of agitated grains, in which granular fluctuation velocity is not induced by fluid turbulence, has elicited relatively few experiments [1,2], in contrast with thermal conduction through static packings, which have received greater attention [3]. In Part I, we outlined a theory for such heat transfer by focusing on a generic fluid-particle system with uniform solid volume fraction v and "granular temperature" Θ, but without an average relative velocity between fluid and solids [4]. (The granular temperature has units of fluctuation velocity squared and measures granular agitation.) We considered grains of a single diameter d, density ρ_s, mass $m = (\pi/6)\rho_s d^3$, specific heat c_s and material conductivity k_s uniformly suspended in a fluid of density ρ_g, specific heat per mass c_g, conductivity k_g and viscosity μ, confined between two parallel flat isothermal walls at different temperatures and separated by the distance L. We showed that grains enhance the heat flux q transferred through these walls above its value q_0 in the clear fluid at rest according to

$$\frac{q}{q_0} = \left(\frac{K_{gt}}{k_g}\right)\left[\frac{1 + \frac{K_s}{K_{gt}}}{1 + \frac{K_s}{K_{gt}}\frac{\tanh(L^\dagger/2)}{(L^\dagger/2)}}\right], \tag{1}$$

where

$$K_s = \frac{\rho_s c_s d\sqrt{\Theta}}{(9\sqrt{\pi})g_{12}}\left(\frac{1}{1 + 2Kn}\right) \tag{2}$$

is a thermal self-diffusivity of the agitated grains, $g_{12}(v)$ is the Carnahan–Starling pair distribution [5]; and $Kn = \lambda_s/L$ is a Knudsen number accounting for the relative size of the granular mean free path $\lambda_s = d/[6\sqrt{2}vg_{12}]$ and L. In Eq. (1),

$$K_{gt} = k_{gt}f_M(v; \xi_{st}) \tag{3}$$

is the conductivity of the gas–solid mixture with $\xi_{st} \equiv k_s/k_{gt}$;

$$\frac{k_{gt}}{k_g} = 1 + \omega\frac{9\sqrt{\pi}}{Pr_t}\left(\frac{\rho_g c_g}{\rho_s c_s}\right)f_M(v; \xi_s) \times g_{12}(1 + 2Kn)\left(\frac{K_s}{K_g}\right) \tag{4}$$

is the molecular conductivity of the gas augmented by particle-induced velocity fluctuations, where $Pr_t \simeq 0.9$ is a turbulent Prandtl number and $\xi_s \equiv k_s/k_g$; and

$$K_g = k_g f_M(v; \xi_s) \tag{5}$$

is the mixture conductivity at rest evaluated at the bulk solid volume fraction v and ξ_s. To evaluate mixture conductivities, we adopted the function recommended by Meredith and Tobias [6],

$$f_M(v; \xi) = \frac{A_1 - 2v + A_2 - 2.133A_3}{A_1 + v + A_2 - 0.906A_3}, \tag{6}$$

where $A_1 = (2 + \xi)/(1 - \xi)$, $A_2 = 0.409v^{7/3}(6 + 3\xi)/(4 + 3\xi)$, $A_3 = 3v^{10/3}(1 - \xi)/(4 + 3\xi)$. In Eq. (1), the distance between hot and cold isothermal walls is made dimensionless using

$$L^\dagger = \frac{L}{d}\sqrt{\frac{12vNu}{(K_{gt}/k_{gt})}f_1 f_2\left(1 + \frac{K_{gt}}{K_s}\right)}, \tag{7}$$

in which the particle Nusselt number Nu is based on k_{gt} and grain radius, and remains unity. The function

* Corresponding author. Tel.: +1 (607) 255 4193; fax: +1 (607) 255 1222.
E-mail address: michel.louge@cornell.edu (M. Louge).

Nomenclature

a_0	vibration amplitude
a_v, b_v, c_v, d_v	constants in Eq. (8)
A, A_h	individual heater surface areas
A_1, A_2, A_3	functions in Eq. (6)
c_g, c_s	fluid, solid specific heats per mass
d	grain diameter
e, e_w	particle, wall restitution
E_1, E_2, E^*	stiffnesses
f	vibration frequency
f_2, f_3, f_4	granular dynamics functions of v
g	gravitational acceleration
g_{12}	binary sphere pair distribution
h	particle heat transfer coefficient
h_{c1}, h_{c2}, h_e, h_b	wall heat transfer coefficients
H	volumetric rate of heat exchange
I	integral of solid volume fraction
k_g, k_s	fluid, solid thermal conductivities
k_{eff}	effective thermal conductivity
k_t, k_{gt}	turbulent, total fluid conductivities
K_g, K_s	mixture, solid-phase conductivities
K_{gt}	augmented mixture conductivity
L	thermal wall-to-wall distance
L_0	reference width in Eq. (8)
$L^\dagger$	relative length scale in Eq. (7)
m	grain mass
M	constant in κ
N	number of realizations
P_s	granular pressure
q_0, q	clear gas, suspension wall fluxes
q^+, q^-	heat fluxes at hot, cold walls
Q_s	steady heat rate supplied
R_b	box thermal resistance
S_b	box external area
t	time
T_g, T_s	fluid, solid thermal temperatures
T_∞,	ambient temperature
T^+, T^-	temperatures of hot and cold walls
v_i	grain fluctuation velocity along i
x, y, z	cartesian coordinates
X, Z	wall-to-wall distances
z_c	filling height at v_c

Greek symbols

β_0, β_{0w}	particle, wall tangential restitutions
γ	granular energy collisional dissipation rate

Θ	granular temperature
ι	variable of integration
κ	conductivity of granular fluctuation energy
λ_s	grain mean free path
μ_s, μ_w	particle, wall friction coefficients
μ	fluid viscosity
v	solid volume fraction
v_f, v_c	freezing, randomly jammed values of v
ξ_s	k_s/k_g
ξ_{st}	k_s/k_{gt}
ξ_1	first root of $\xi/\tan\xi = 1 - Bi$
Ξ	collision number wall flux
ρ_g, ρ_s	fluid, solid material densities
σ_1, σ_2	Poisson's ratios
Ψ	flux of granular fluctuation energy
ω	constant in Eq. (4)
Ω	slope in Eq. (42)

Dimensionless groups

Bi	Biot number
Da	Damköhler second ratio
Fo_c	time-of-flight Fourier number
Kn	Knudsen number
Nu	particle Nusselt number
Pr	Prandtl number
Pr_t	turbulent Prandtl number
Ra	Rayleigh number
Re	particle Reynolds number
Γ	dimensionless acceleration
Λ	dimensionless vibration self-diffusivity (Eq. (31))
Υ	vibration Froude number

Scripts

$\dagger, ^*$	dimensionless
–	average along z
g, s	gas, solid
air, He	air, helium
th, nx, ex	theory, numerical simulation, experiment

$$f_1(v; L/d) = \frac{1 + v(1 - e^{-L/L_0})(b_v + a_v v)}{1 + v(1 - e^{-L/L_0})(d_v + c_v v)}, \tag{8}$$

in which the parameters $L_0/d \approx 12.8$, $a_v \approx 1385$, $b_v \approx 230$, $c_v \approx 4370$, and $d_v \approx 327$ arise from our integration of HAB theory [7], captures effects of spatial ordering imposed by the thermal walls on K_g and the volumetric rate of heat exchange $\widetilde{H}$ between solids and fluid. The function

$$f_2(Bi, Fo_c) \approx \exp(-\zeta_1^2 Fo_c) \times \left[1 - \frac{Bi}{5} + \frac{3}{520}Bi^2 + \frac{99}{13000}Bi^3 \right] \tag{9}$$

captures the dependence of $\widetilde{H}$ on the grain Biot number

$$Bi = Nu/\xi_{st} \tag{10}$$

to a good approximation for $Bi < 1.3$, where the eigenvalue $\zeta_1 \approx \sqrt{3Bi}[1 - Bi/10 + Bi^2/156]$ and the Fourier number based on mean granular time-of-flight is related to K_s/K_g using

$$Fo_c = \frac{\xi_s}{54 v g_{12}^2 (1 + 2Kn)(\frac{K_s}{K_g}) f_M(v; \xi_s)}. \tag{11}$$

The Lattice–Boltzmann numerical simulations of Verberg and Koch indicate that, in dense suspensions of spheres, the gas Reynolds stress is proportional to strain rate and $\rho_g \Theta^{1/2} d$ [8]. Equivalently, we suggested in Part I that the parameter ω in Eq. (4) is a function of v that must vanish at $v = 0$ [4]. We then adopted Verberg and Koch's measurement of $\omega = 0.037$ at $v = 0.3$ and, in the absence of published measurements at other volume fractions, assumed $\omega = (0.037/0.3)v$.

In short, to capture effects of particle-induced gas velocity fluctuations on heat transfer, our approach is to raise the gas conductivity from its molecular value k_g to k_{gt}, to calculate k_{gt} from the measurements of Verberg and Koch [8] in numerical simulations of dense gas–solid suspensions, and to account for the resulting conductivity augmentation in the mixture conductivity, the particle Biot number, and the gas–solid heat exchange rate. We adopt this approach rather than invoking an empirical correlation [9] that raises the Nusselt number of an individual sphere with a particle Reynolds number based on fluctuation velocity,

$$Re = \frac{9\sqrt{3\pi}g_{12}}{Pr}\left(\frac{\rho_g c_g}{\rho_s c_s}\right) \times f_M(v; \xi_s)\left(\frac{K_s}{K_g}\right)(1 + 2Kn),\tag{12}$$

where $Pr = \mu c_g/k_g$ is the Prandtl number of the gas.

An important assumption of our thermal theory is that grains do not exchange any appreciable heat during their ephemeral collisions among themselves or with the wall. This is the case if

$$\frac{\rho_s^{1/5}E^{*4/5}dc_s}{\Theta^{3/10}k_s} \gg 1,\tag{13}$$

where $E^{*-1} = [(1 - \sigma_1^2)/E_1 + (1 - \sigma_2^2)/E_2]$ combines the Young's moduli E_i and Poisson's ratios σ_i of the two impact protagonists. This assumption implies that, although grains can transport heat through self-diffusion (Eq. (2)), they must first exchange this heat with the fluid, before it can be transferred by the fluid to the wall. These two serial processes resemble the competition between diffusion and chemical kinetics in diffusion flames, and are similarly arbitrated by a Damköhler second ratio

$$Da = \frac{(K_g/K_s)(L^\dagger/2)}{\tanh(L^\dagger/2)},\tag{14}$$

which delineates two asymptotic situations. At high Da, self-diffusion dominates q/q_0 in a regime that we call the "diffusion limit", for which the thermal temperatures of fluid and solid are identical, and thus assumption (13) is not as crucial. At low Da, self-diffusion no longer matters directly, but instead q/q_0 is governed by the ability of individual spheres to exchange heat with the fluid through the difference between their thermal temperature and that of the fluid. In this "exchange limit", granular agitation can still play a role, as mentioned earlier, by raising the mixture conductivity from K_g to K_{gt}, the particle Biot number, and the gas–solid exchange rate through k_{gt}. These effects are captured to a good approximation by Eqs. (1)–(11), without having to integrate the governing thermal equations numerically.

In Part II, we test this theory with an experiment consisting of an insulated vibrated box containing agitated spheres in air between two isothermal flat walls, one cooled and the other heated. The thermal heat flux is inferred from the electrical energy supplied to the heated wall at steady-state. We begin Part II with a description of the experiment. Further details are provided in Chen's doctoral thesis [10]. To compare experimental data and theory, we derive a model for solids agitation in the box, which gravity renders inhomogeneous in the vertical direction.

2. Apparatus

To produce a dense, relatively uniform suspension of agitated particles in the laboratory without an average relative velocity between gas and solids, a simple way is to shake spheres in a rectangular box. Such shaking must be sufficient to agitate the spheres without creating excessive granular condensation at the base of the box. Following a brief description of the apparatus in Section 2.1, we outline a simple analysis of granular shaking in Section 2.2.

In evaluating the heat flux q, the principal challenge is to account for thermal flows that do not traverse the suspension. Our strategy is to minimize conduction through, and convection away from, the box walls. However, because such parasitic heat flows cannot be eliminated, we employ a measurement strategy that keeps them nearly constant, maintains a nearly two-dimensional temperature field where measurements are performed, and extracts q from a simple lumped-parameter model of the box and its contents. We summarize this heating strategy in Section 2.3.

2.1. Description

Fig. 1 is a conceptual sketch of the apparatus. A sinusoidal vibration of amplitude a_0 and frequency $f = 50$ Hz is produced in the upward vertical direction z by a VTS-100 shake table driven by a function generator and capable of delivering a 450 N peak force. We calibrate and verify the table displacement time-history using a capacitance probe system of precision better than 10 μm and bandwidth 0–4 kHz. Each experiment is run at the five amplitudes $a_0 = 0.72, 0.96, 1.27, 1.69$, and 1.96 mm.

The thermal heat flux traverses the suspension from the heating (right) to the cooling (left) surfaces separated by a distance $L = 25$ mm along y. The depth along x is bounded by two flat, vertical insulated walls a distance $X = 76$ mm apart made of RESCOR 360HS ceramic board with a relatively low conductivity of 0.07 W/m K and thickness of 15–30 mm. Spheres are agitated by colliding among themselves and with bumps on the top and bottom walls consisting of rectangular brass bars of 4 mm width spanning the entire depth. The bars are thin and hollow to minimize fatigue of the ceramic in which they are imbedded, while increasing its stiffness. They are separated by ceramic-filled gaps of 2 mm to reduce wall conduction along y. The vertical distance between opposite bars is $Z = 25$ mm. The box is held together by threaded metal braces outside the ceramic walls. External dimensions are $105 \times 60 \times 85$ mm³ along x, y and z.

We conduct experiments with acrylic spheres of 2, 3.2 and 4 mm diameter, and with aluminum spheres of 3.2 mm diameter. The latter have a very low Biot number ($\sim 1.5 \times 10^{-4}$ at $k_t = 0$) and a large k_s that has the potential to generate high mixture conductivities. The former have a higher $Bi \sim 0.2$ at $k_t = 0$, so that the correction in Eq. (9) can differ significantly from unity as k_t grows. In separate experiments, we employ the technique of Foerster et al. [11,12] to measure impact parameters. For binary collisions, these include the coefficients of normal kinematic restitution e, friction μ_s and tangential restitution β_0. For impacts of those spheres with metal bumps, the respective parameters are e_w, μ_w and β_{0w}. They are listed in Table 1. A disadvantage of aluminum spheres is that they dissipate much energy in collisions and, as we will later discuss, their suspensions are more likely to collapse in the vibrated box. Properties of gases used are shown in Table 2.

Fig. 2 is a sketch of the assembly. Heat is generated by three square Watlow thick-film electrical heaters with negligible capac-
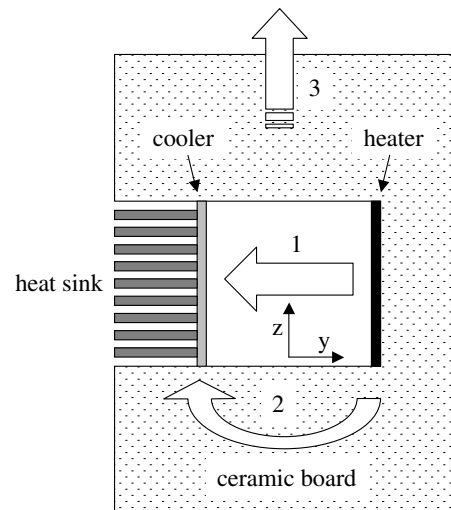

Fig. 1. Sketch of a cross-section of the vibrated box in the (y,z) plane. Dimensions are not to scale. Large arrows labeled 1, 2 and 3 mark heat energy paths corresponding to the three terms in Eq. (41).

Table 1
Grain impact parameters and properties

Material	e	μ_s	β_0	e_w	μ_w	β_{0w}	ρ_s (kg/m^3)	c_s (J/kg K)	k_s (W/m K)
Acrylic	0.93	0.12	0.35	0.965	0.22	0.28	1180	1400	0.14
Aluminum	0.45	0.1	0.3	0.5	0.1	0.3	2700	900	180

Table 2
Gas properties at 320 K

Gas	ρ_g (kg/m^3)	c_g (J/kg K)	k_g (W/m K)	μ (kg/m s)
Air	1.12	1010	0.028	1.9×10^{-5}
Helium	0.157	5200	0.159	2.1×10^{-5}

itance or inductance. To minimize temperature variations on the heating surface exposed to the suspension, each heater is covered over its entire surface of area $A = 25.4 \times 25.4$ mm^2 by a square copper plate bonded using highly conductive thermal paste. A copper-constantan thermocouple is inserted beneath each plate. The thermal flux is inferred from the power supplied to the central heater using the lumped-parameter model discussed in Section 2.3. A Watlow "Series 96 1/16 DIN" controller maintains the thermocouple temperature at $T^+ = 333$ K $\pm$ 0.1 K by supplying short $\lesssim 200$ ms bursts of 60 Hz AC voltage to the heater. A National Instrument DAQ-1200 card mounted in a laptop computer acquires power consumption data at a sampling rate of 4 kHz using the LabView software. The laptop is operated on batteries to minimize electrical supply noise.

The two side heaters act as a "guard" making the thermal problem nearly two-dimensional. To that end, they are jointly set to the operating temperature of the central heater with a separate Watlow controller. Because the three adjacent heaters are separated by a thin layer of RESCOR 360HS ceramic, and because great care is taken to equate their temperatures, we calculate that conduction from the central heater along the x-direction is <1% of the heat flux $|q|$ traversing the box.

The heat flux is absorbed by three Melcor CP0.8-127-06L thermoelectric coolers of 24.6×24.6 mm^2 inserted between a single copper plate exposed to the suspension and external aluminum fins air-cooled by forced convection. A Melcor MTCA-9060 controller maintains the plate temperature at four possible steady values $T^- = 293, 303, 313$ or 323 K monitored by three YSI series 44,008 thermistors inserted beneath the plate. For these operating temperatures and at the effective emissivity of the suspension and the polished copper plates, the radiation flux emitted by the central heater or received by the coolers is <1% $|q|$.

The thermal response time of the system is relatively high, thus making readings stable, but compelling us to wait before a steady-state is achieved. At worst, when heater and cooler are suddenly turned off, the box at rest returns to the ambient temperature on a $1/e$ time of approximately 13 min.

2.2. Shaking

A challenge of our experiments is that gravity and energy dissipated in collisions create vertical inhomogeneities in granular agitation and solid volume fraction, thus complicating the interpretation of thermal data with a theory meant for uniform Θ and ν. Gravity draws grains to the bottom unless agitation is high enough to minimize the resulting imbalance in solid volume fraction. In the worst case, an insufficient vibration energy input can collapse the suspension. In this section, we describe a simple one-dimensional granular dynamics model capturing these effects, and we briefly outline discrete-element-modeling (DEM) numerical simulations to infer the granular temperature in experiments. Other simulations and more detailed analyses may be found, for example, in Refs. [13–16].

To compare measurements of q/q_0 with predictions of the theory, we first evaluate the self-diffusive conductivity K_s of the solid-phase using Eq. (2). To that end, we compute the average dimensionless granular temperature $\overline{\Theta}^* \equiv \overline{\Theta}/(a_0 2\pi f)^2$ in
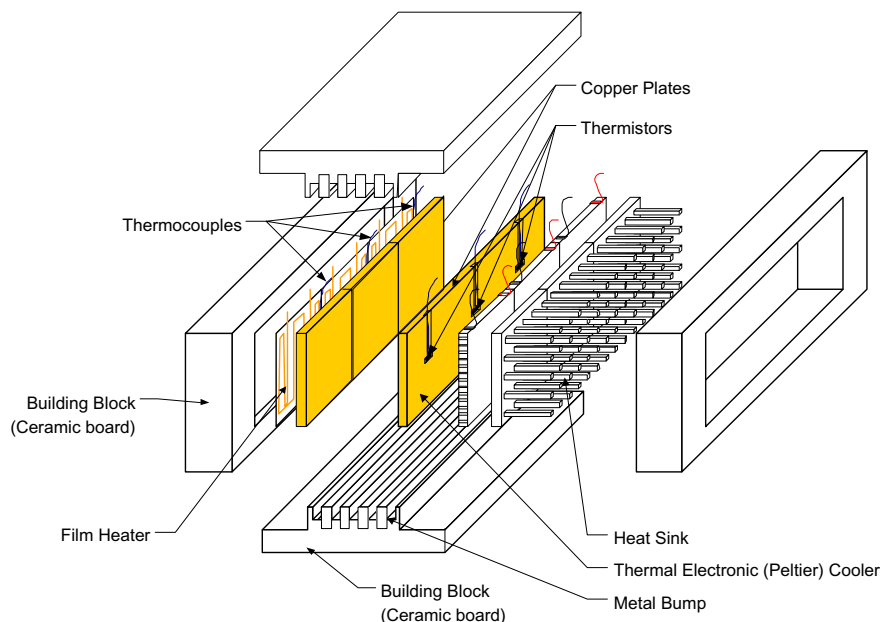
Fig. 2. Assembly sketch of the vibrated box without the ceramic retaining side walls perpendicular to x.

numerical simulations employing the DEM hard-sphere algorithm described by Hopkins and Louge [17]. The algorithm detects collisions once spheres have overlapped slightly and, for the sake of computing speed, periodically optimizes the time step between consecutive realizations to achieve a small average tolerated overlap. It calculates post-impact velocities based on the normal restitution, friction and tangential restitution parameters recorded in independent collision experiments [11,12].

We assume that the N grains in the box have no mean velocity, and compute their mean temperature over several realizations

$$\overline{\Theta} = \frac{1}{N} \sum_{i=1}^{N} \left(\frac{v_x^2 + v_y^2 + v_z^2}{3} \right), \tag{15}$$

where v_x, v_y and v_z are grain velocities in the three cartesian directions. The rectangular simulation domain is bounded with flat walls separated by the same relative distances Y/d and Z/d as in the experiments. For simplicity, the domain has periodic boundaries along x separated by L. The virtual box is vibrated along z at the dimensionless acceleration $\Gamma \equiv (2\pi f)^2 a_0/g$, and contains spheres with impact parameters in Table 1. Because collision velocities on the order of $0.02 < \sqrt{\Theta} < 1.1$ m/s are within the range where we observe constant impact parameters [11,12], we expect $\sqrt{\Theta}$ to scale with $(2\pi f a_0)$, unlike the more complicated scaling that Falcon, et al have reported [18].

To model the granular system, we consider frictionless spheres colliding between two horizontal planes vibrating in unison as $z_0 = a_0 \sin(2\pi ft)$. Quantities only vary along z. The mean volume fraction in the domain is

$$\bar{v} = \frac{1}{Z} \int_0^Z v \, dz, \tag{16}$$

where the overbar denotes spatial averaging along z. The granular pressure is

$$P_s = f_4(v)\rho_s\Theta. \tag{17}$$

In the presence of the gravitational acceleration g, a vertical hydrostatic gradient develops. Neglecting contributions from the gas,

$$\frac{dP_s}{dz} = -\rho_s v g. \tag{18}$$

Without stress work or convection, the balance of fluctuation energy for nearly elastic, frictionless spheres is

$$0 = -\frac{d\psi}{dz} - \gamma, \tag{19}$$

where

$$\psi = -\kappa \frac{d\Theta}{dz} \tag{20}$$

is the flux of granular fluctuation energy across horizontal planes, with conductivity $\kappa = f_2(v)\rho_s d\sqrt{\Theta}$. In Eq. (19), $\gamma = f_3(v)(1 - e^2) \rho_s\Theta^{3/2}/d$ is the volumetric rate of collisional dissipation. (In this equation, we neglect the role of the gas in dissipating Θ [19,20].) For nearly elastic, frictionless spheres, Jenkins and Richman [21] provided expressions for the functions $f_2(v) = (4/\sqrt{\pi})Mv^2 g_{12}$ with $M \equiv 1 + (9\pi/32)[1 + 5/(12vg_{12})]^2$, $f_3(v) = (12/\sqrt{\pi})v^2 g_{12}$, and $f_4(v) = v(1 + 4vg_{12})$.

We make the governing equations dimensionless by defining $z' \equiv z/Z$, $P_s' \equiv P_s/(\rho_s g d)$, $\Theta' \equiv \Theta/(gd)$, and $\psi' \equiv \psi(Z/d)/[\rho_s(gd)^{3/2}]$. We write the result as a system of four coupled non-linear ODEs,

$$\frac{dP_s'}{dz'} = -v\frac{Z}{d}, \tag{21}$$

$$\frac{d\Theta'}{dz'} = -\frac{\psi'}{f_2\Theta'^{1/2}}, \tag{22}$$

$$\frac{d\psi'}{dz'} = -f_3(1 - e^2)\left(\frac{Z}{d}\right)^2 \Theta'^{3/2}, \tag{23}$$

and

$$\frac{dI}{dz'} = v. \tag{24}$$

We use the integral $I \equiv \int_{i=0}^{z'} v(i) \, di$, where i is a variable of integration representing z', to enforce the average solid volume fraction in the box. At each step of integration, the program determines v from P_s' and Θ' by inverting numerically the function $f_4(v) = P_s'/\Theta'$ from Eq. (17) with a fast interpolation look-up table.

We prescribe boundary conditions at the horizontal vibrated walls, which supply a flux of fluctuation energy to the suspension. Richman [22] derived a theoretical expression for ψ through a randomly vibrated bumpy boundary. Because the geometry and operation of our box are different, we take a heuristic approach based on a simpler scaling for ψ that produces reasonable agreement with numerical simulations. Specifically, we assume that grains acquire a fluctuation velocity proportional to the product of the normal restitution coefficient e_w and the velocity amplitude of the wall, and write the corresponding flux

$$\psi \sim m(2\pi f a_0 e_w)^2 \Xi, \tag{25}$$

where the number of collisions per unit area of the wall and unit time is [23]

$$\Xi = \left(\frac{3\sqrt{2}}{\pi^{3/2}}\right)\left(\frac{\Theta^{1/2}}{d^3}\right)\left[\frac{v(1 + 2v)}{(1 - v)^2}\right]. \tag{26}$$

Chen derived a more rigorous expression for ψ involving all wall impact parameters [10]. However, his more detailed analysis, which produced different expressions of ψ for the inward and outward strokes of the vibrated wall, only captured qualitative trends for variations of ψ with v and impact parameters.

If grains collide with both top and bottom walls, we write the corresponding dimensionless boundary fluxes as

$$\psi'(z' = 0, 1) = \pm\sqrt{\frac{1}{2\pi}}\left(\frac{Z}{d}\right)\Upsilon\left[\frac{v(1 + 2v)}{(1 - v)^2}\right]\Theta'^{1/2}, \tag{27}$$

where the plus and minus signs correspond to $z' = 0$ and $z' = 1$, respectively, and indicate that both boundaries supply fluctuation energy to the suspension. In this system, there are four dimensionless parameters, namely Z/d, $\bar{v}$, e and $\Upsilon \equiv (2\pi f a_0 e_w)^2/gd$. Υ is related to the relative vibrational acceleration Γ, which is invoked more often in studies of vibrated grains. We integrate Eqs. (21)–(24) numerically with MATLAB's bvp4c code, subject to the two boundary conditions (27), and to $I = 0$ at $z' = 0$ and $I = 1$ at $z' = 1$.

If Υ or e are too small, or if Z/d is too large, as in experiments with 2 mm acrylic or 3.2 mm aluminum spheres, the suspension may not reach the top of the box. In such "collapsed" situation, we no longer prescribe ψ at $z' = 1$, but instead write that the suspension weight is entirely borne by the bottom wall,

$$P_s'(z' = 0) = \bar{v}\frac{Z}{d}. \tag{28}$$

For such experiments, the expression of Carnahan and Starling [5] for the pair distribution function

$$g_{12} = \frac{(2 - v)}{2(1 - v)^3} \tag{29}$$

is no longer valid if the local v exceeds the "freezing" value $v_f \approx 0.49$; in that event, we invoke Torquato's extension for $v > v_f$,

$$g_{12} = \frac{(2 - v_f)}{2(1 - v_f)^3} \times \frac{(v_c - v_f)}{(v_c - v)}, \tag{30}$$

where $v_c \approx 0.64$ is the volume fraction of the random jammed state [24].

Once profiles $v(z')$ and $\Theta'(z')$ are established, we use Eq. (2) to find vertical variations of

$$\frac{K_s}{K_g} = \frac{\Lambda \Theta'^{1/2}}{(1 + 2Kn)(9\sqrt{\pi})g_{12}f_M(v; k_s/k_g)}, \tag{31}$$

and we substitute the results in Eqs. (1) and (3)–(11) to evaluate how Bi, Fo_c, Kn, k_{gt}, ξ_{st}, K_{gt}, $L^\dagger$ and, ultimately, q/q_0 vary along z'. Thus, a new dimensionless number $\Lambda \equiv \rho_s c_s d \sqrt{gd}/k_g$ appears when gravity is present. Because the suspension behaves as a medium with conductivity varying in the direction perpendicular to the temperature gradient, the total flux is obtained by summing the contributions of elementary slices of dimensionless height dz',

$$\frac{\bar{q}}{q_0} = \int_{z'=0}^{1} \frac{q(z')}{q_0} \, dz'. \tag{32}$$

For consistency with Eq. (15), we evaluate $\overline{\Theta}$ as a weighted average involving the local solid volume fraction,

$$\overline{\Theta} = \int_0^Z \Theta v \, dz / \int_0^Z v \, dz. \tag{33}$$

Fig. 3 contrasts vertical profiles for a situation in which grains are well agitated through the height of the box, to another in which the suspension has begun to collapse to the bottom. In the first (solid lines), the flux ratio q/q_0 is nearly uniform. In the second (dashed lines), the collapse creates a mildly agitated region of high solid volume fraction near the base, where the sharp rise in q/q_0 is a result of much higher local values of K_g/k_g. In the extreme case when $\Theta \to 0$, the entire granular medium fills the bottom of the box to a height $z_c = Z\bar{v}/v_c$ with mixture conductivity $K_g/k_g = f_M(v_c; \xi_s)$, and Eq. (32) tends to

$$\frac{\bar{q}}{q_0} \to \left(\frac{z_c}{Z}\right) f_M(v_c; \xi_s) + \left(1 - \frac{z_c}{Z}\right). \tag{34}$$

Because experiments with the collapsed system are dominated by K_g/k_g, they are not as instructive for studying the thermal behavior of agitated grains. In that case, Vargas and McCarthy [3], for example, offer a better account of the relevant heat transfer, which crucially depends on static stresses applied to the granular assembly that are not considered here.

As Tables 3–6 indicate, although the numerical simulations have more realistic geometry and impact parameters than the

Table 3
Experimental data for 4 mm acrylic spheres

L/d	$\bar{v}$	Γ	$\overline{\Theta}^*_{th}$	$\overline{\Theta}^*_{ns}$	K_s/K_g	$(\bar{q}/q_0)_{th}$	$(\bar{q}/q_0)_{ex}$
6.4	0.065	7.2	2.1	2.9	2900	3.3	4.3
		9.7	2.1	1.9	3200	3.6	4
		13	2.1	1.7	4000	4	4.2
		17	2.1	2.4	6300	4.6	5.6
		20	2.1	3.8	9100	4.9	**6**
6.4	0.13	7.2	1.1	1.3	1800	4.9	4
		9.7	1.1	1.5	2600	5.4	3.5
		13	1.1	1.3	3100	6.2	3.9
		17	1.1	1.1	3900	7.2	**4.5**
		20	1.1	1.3	4800	7.8	**5.6**
6.4	0.195	7.2	0.68	0.91	1200	6.3	5.7
		9.7	0.71	0.83	1500	7.1	5.8
		13	0.73	0.84	2100	8.2	5.6
		17	0.74	0.88	2800	9.5	**6.3**
		20	0.74	0.79	3100	10	**8**
6.4	0.26	7.2	0.49	0.67	790	7.6	8
		9.7	0.53	0.53	930	8.7	6.9
		13	0.55	0.65	1400	10	7.7
		17	0.56	0.63	1800	12	8.6
		20	0.56	0.71	2200	13	10.2
6.4	0.325	7.2	0.39	0.5	500	8.9	5.5
		9.7	0.43	0.48	650	10	7.3
		13	0.45	0.47	840	12	10.2
		17	0.45	0.58	1300	14	**11.3**
		20	0.45	0.68	1600	15	**12.2**
6.4	0.39	7.2	0.33	0.46	330	10	5.9
		9.7	0.37	0.4	410	12	8.1
		13	0.38	0.41	550	14	**9.3**
		17	0.38	0.54	850	16	**13.1**
		20	0.38	0.56	1000	17	**13.1**

The subscripts "th", "ns", and "ex" refer to theory, numerical simulations and experimental data, respectively. Values of $(q/q_0)_{ex}$ in boldface represent conditions for which $\gamma L/2 > 0.1|q|$. $\overline{\Theta}^*_{th}$ and $\overline{\Theta}^*_{ns}$ are average granular temperatures made dimensionless with $(2\pi f a_0)^2$ and calculated, respectively, from the model using Eq. (33), and from simulations using Eq. (15). K_s/K_g is calculated from Eqs. (2) and (5) using $\bar{v}$ and $\overline{\Theta}^*_{ns}$ from numerical simulations. $(\bar{q}/q_0)_{th}$ is the average flux ratio calculated with the theory of Eq. (1) and averaged in the vertical direction with Eq. (32); $(\bar{q}/q_0)_{ex}$ is experimental data calculated with Eq. (43).

model, the mean granular temperatures measured in simulations using Eq. (15) agree well with model predictions of Eq. (33), except
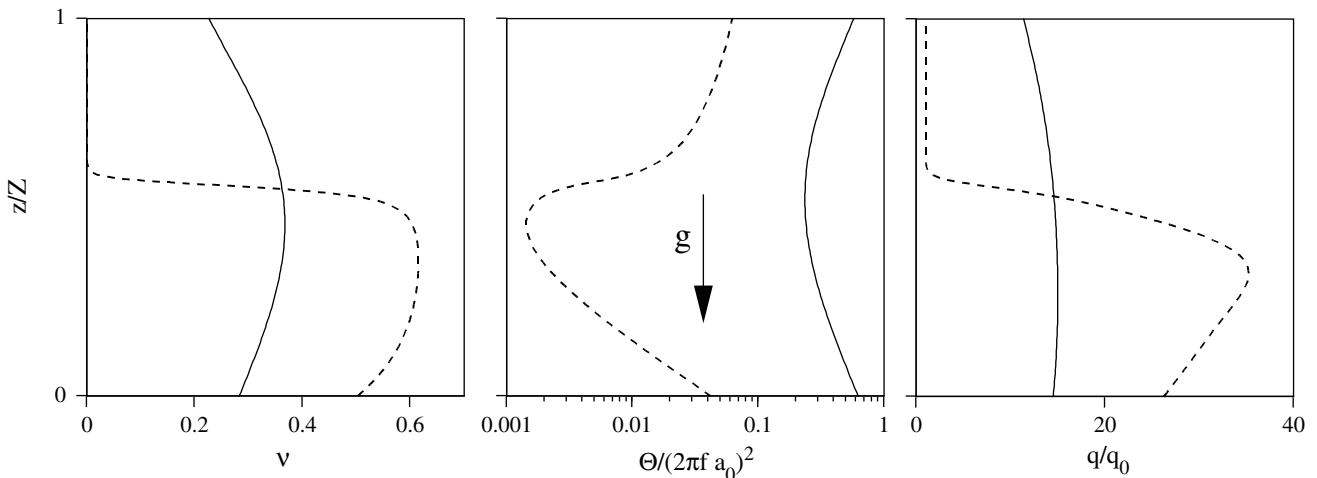
Fig. 3. Vertical profiles of solid volume fraction v, dimensionless granular temperature $\Theta/(2\pi f a_0)^2$ and flux ratio q/q_0 at a vibration amplitude $a_0 = 1.69$ mm and frequency $f = 50$ Hz ($\Gamma = 17$) for acrylic (solid lines, $\Upsilon = 8.4$) and aluminum (dashed lines, $\Upsilon = 2.2$) spheres of 3.2 mm diameter ($L/d = Z/d = 7.9$) at $\bar{v} = 0.325$. Relevant gas and solid properties to calculate q/q_0 from Eqs. (1)–(11) are shown in Tables 1 and 2. The arrow points toward the direction of gravity.

Table 4
Experimental data for 3.2 mm acrylic spheres

L/d	$\bar{v}$	Γ	$\overline{\Theta}^*_{th}$	$\overline{\Theta}^*_{ns}$	K_s/K_g	$(\bar{q}/q_0)_{th}$	$(\bar{q}/q_0)_{ex}$
7.9	0.065	7.2	1.7	1.8	2000	3.6	3.5
		9.7	1.7	2.1	2800	3.9	4
		13	1.7	1.7	3300	4.3	3.5
		17	1.7	1.7	4500	4.7	4.6
		20	1.7	1.6	5010	5.1	4.9
7.9	0.13	7.2	0.8	0.83	1200	5.3	5.3
		9.7	0.82	0.92	1700	5.8	5.2
		13	0.84	0.91	2200	6.5	5.3
		17	0.84	0.8	2800	7.4	5.9
		20	0.85	0.81	3200	7.9	7
7.9	0.195	7.2	0.5	0.64	830	6.8	7.3
		9.7	0.52	0.69	1200	7.6	7.2
		13	0.55	0.48	1300	8.5	6.5
		17	0.56	0.55	1800	9.8	8.1
		20	0.56	0.54	2100	11	**9.2**
7.9	0.26	7.2	0.35	0.49	550	8.2	7.3
		9.7	0.38	0.44	690	9.2	7.8
		13	0.41	0.41	890	10	8.7
		17	0.42	0.42	1200	12	11.7
		20	0.42	0.36	1300	13	13.3
7.9	0.325	7.2	0.27	0.32	320	9.5	6.7
		9.7	0.3	0.33	430	11	7.3
		13	0.33	0.33	570	12	7.6
		17	0.34	0.34	770	14	**11.5**
		20	0.34	0.33	880	15	**15.5**
7.9	0.39	7.2	0.21	0.26	200	11	6.3
		9.7	0.26	0.26	270	12	7.6
		13	0.28	0.28	370	14	8.3
		17	0.28	0.29	500	16	**11.7**
		20	0.28	0.3	580	17	**18**

Symbols, see Table 3.

Table 5
Experimental data for 2 mm acrylic spheres. Symbols, see Table 3

L/d	$\bar{v}$	Γ	$\overline{\Theta}^*_{th}$	$\overline{\Theta}^*_{ns}$	K_s/K_g	$(\bar{q}/q_0)_{th}$	$(\bar{q}/q_0)_{ex}$
12.7	0.065	7.2	1	1.1	1100	4.7	5
		9.7	1	1	1400	5.1	5
		13	1	1.1	1900	5.4	4.9
		17	1	1	2500	5.8	5.4
		20	1	1	2800	6.1	6.7
12.7	0.13	7.2	0.43	0.4	550	6.6	6
		9.7	0.41	0.47	790	7.2	7.5
		13	0.44	0.45	1000	7.9	7.5
		17	0.46	0.44	1300	8.7	8.2
		20	0.47	0.41	1500	9.1	9.4
12.7	0.195	7.2	0.27	0.19	290	8.3	4.7
		9.7	0.24	0.19	390	9	8.1
		13	0.24	0.19	520	9.9	10.4
		17	0.29	0.2	700	11	11.7
		20	0.29	0.23	870	12	13.9
12.7	0.26	7.2	0.18	0.14	180	9.7	6.3
		9.7	0.17	0.13	240	11	11.7
		13	0.16	0.13	310	11	13.2
		17	0.21	0.13	420	13	15.1
		20	0.22	0.13	490	14	16.8
12.7	0.325	7.2	0.135	0.092	110	11	5.6
		9.7	0.13	0.1	150	12	11.2
		13	0.119	0.091	190	13	15.4
		17	0.17	0.1	270	15	17.9
		20	0.17	0.1	300	16	19.3
12.7	0.39	7.2	0.104	0.081	70	11	5.6
		9.7	0.1	0.075	91	13	12.1
		13	0.095	0.07	120	15	17.3
		17	0.143	0.069	150	17	19.2
		20	0.145	0.064	170	18	22.9

in certain collapsed situations. The model is particularly useful at relatively small values of Z/d, for which vertical profiles are pronounced. In that case, Fig. 4 compares model and simulations for $\overline{\Theta}^* \equiv \overline{\Theta}/(2\pi f a_0)^2$ versus Υ for 2 mm acrylic spheres at two values of $\bar{v}$. At $\bar{v} = 0.065$, the suspension is agitated through the range of z/Z. At $\bar{v} = 0.39$, it collapses partially and achieves a much lower $\overline{\Theta}^*$. Curiously, for $\bar{v} = 0.39$, the model predicts two overlapping solutions in the range $7 \lesssim \Upsilon \lesssim 10$. However, simulations suggests that the more energetic state is not stable.

A simpler calculation allows us to predict the level of granular temperature achieved in nearly homogeneous suspensions, without invoking the numerical model. Assuming that $\Theta \simeq \overline{\Theta}$ and $v \simeq \bar{v}$ are uniform in the box, a balance of fluctuation energy supplied through the two boundaries of area (XL) and consumed in the volume (XLZ) yields $2\psi \sim \gamma Z$, or

$$\overline{\Theta}^* \simeq \frac{1}{3\sqrt{2}} \frac{e_w^2}{(1-e^2)} \frac{(1+2\bar{v})(1-\bar{v})}{(2-\bar{v})\bar{v}} \frac{1}{(Z/d)}. \qquad (35)$$

For experiments with 3.2 and 4 mm acrylic spheres, for which the model predicts nearly uniform v and Θ, Eq. (35) agrees with simulations to better than 28%. Ideally, experiments should be carried out in this nearly homogeneous regime. The best way to do so is to conduct them in microgravity, so issues arising from suspension collapse are avoided.

2.3. Heating strategy

The guard heater described in Section 2.1 minimizes conduction losses in the depth x of the cell, thus making heat transfer nearly two-dimensional in the plane (y,z). However, this technique does not eliminate heat conduction through the walls. Because the porous ceramic box material has a conductivity just above that of air, it transfers heat at a rate comparable to the suspension's. Managing wall conduction is the principal challenge of heat transfer measurements with gas–solid mixtures. Our strategy is to keep such conduction as constant as possible by fixing the heater temperature T^+, and to infer the suspension conductivity from tests at four different cooler temperatures T^-.

Another challenge is that the fluctuation energy dissipated in grain collisions can produce significant heat. To account for this, we add the volumetric rate of collisional dissipation to the thermal balance of the particle phase,

$$0 = -\frac{d}{dy}\left(-K_s \frac{dT_s}{dy}\right) - H + \gamma, \qquad (36)$$

which we solve simultaneously with its counterpart for the gas phase

$$0 = -\frac{d}{dy}\left(-K_g \frac{dT_g}{dy}\right) + H, \qquad (37)$$

subject to the boundary conditions $T_g = T^\pm$ and $dT_s/dy = 0$ at $y = \pm L/2$. In these equations, T_g and T_s are the thermal temperature of the gas and solids, respectively, and H is the average volumetric rate of thermal energy that particles supply to the gas. If $\gamma \neq 0$, a one-dimensional balance of thermal energy reveals that the heat flux $q^- < 0$ crossing the cold plate differs from its counterpart $q^+ < 0$ through the hot wall according to

$$q^+ - q^- = \gamma L. \qquad (38)$$

Because Eqs. (36) and (37) are linear in γ, T_g and T_s, and because $q^+ = q^- = q$ when $\gamma = 0$, one can show that $(q^+ + q^-)/2 = q$, where

Table 6
Experimental data for 3.2 mm aluminum

L/d	$\bar{v}$	Γ	$\overline{\Theta}^*_{\text{th}}$	$\overline{\Theta}^*_{\text{ns}}$	K_s/K_g	$(\bar{q}/q_0)_{\text{th}}$	$(\bar{q}/q_0)_{\text{ex}}$
7.9	0.065	7.2	0.1	0.4	1300	3	3.4
		9.7	0.08	0.25	1300	3.1	4.1
		13	0.07	0.24	1700	3.2	5.5
		17	0.07	0.29	2500	3.3	5.1
		20	0.06	0.37	3300	3.4	7.3
7.9	0.13	7.2	0.035	0.064	420	5.6	8.6
		9.7	0.037	0.05	500	5.5	9.1
		13	0.033	0.051	660	5.4	9
		17	0.03	0.078	1100	5.5	9.5
		20	0.029	0.075	1200	5.5	9.7
7.9	0.195	7.2	0.006	0.026	200	14	10.3
		9.7	0.016	0.024	250	8.8	12
		13	0.019	0.018	290	8.3	8.2
		17	0.018	0.012	310	8.2	9.5
		20	0.017	0.017	440	8.1	11.5
7.9	0.26	7.2	0.001	0.013	100	*49*	7.7
		9.7	0.005	0.01	110	*18*	9.9
		13	0.01	0.022	220	*12*	14.1
		17	0.012	0.011	210	*12*	14.3
		20	0.0115	0.0082	210	*11*	15.6
7.9	0.325	7.2	0.0004	0.008	50	*65*	7.5
		9.7	0.0003	0.0079	67	*64*	8
		13	0.02	0.0099	100	*22*	14.5
		17	0.0292	0.0079	120	*17*	16.2
		20	0.0302	0.0078	130	*16*	16.9
7.9	0.39	7.2	0.0003	0.0076	31	*80*	7.7
		9.7	0.0001	0.0063	37	*80*	9.7
		13	0.0024	0.0058	47	*44*	17.9
		17	0.0054	0.0046	56	*27*	18.5
		20	0.006	0.0092	92	*24*	21

Values of $(\bar{q}/q_0)_{\text{th}}$ in italics denote a suspension predicted to be near complete collapse, and for which $(\bar{q}/q_0)_{\text{th}}$ tends to the value in Eq. (34).
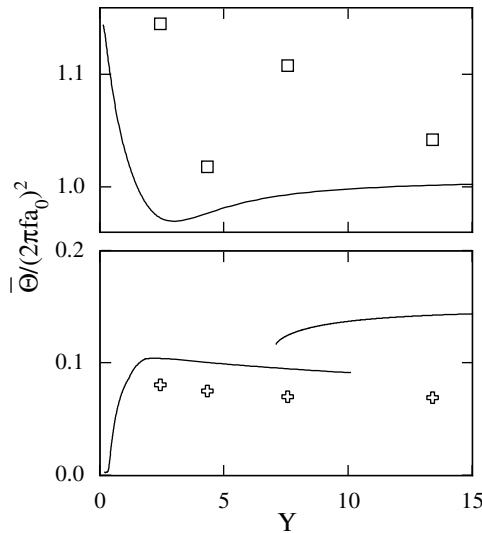
Fig. 4. Mean dimensionless granular temperature $\overline{\Theta}^* \equiv \overline{\Theta}/(2\pi f a_0)^2$ in the box versus $\Upsilon \equiv (2\pi f a_0 e_w)^2/gd$ for 2 mm acrylic spheres ($L/d = Z/d = 12.7$) at $\bar{v} = 0.065$ (top) and $\bar{v} = 0.39$ (bottom). Note the different ranges on the ordinate axis. Lines are predictions of the model in Eqs. (21)–(24). Crosses and squares are data from numerical simulations at $\bar{v} = 0.065$ and $\bar{v} = 0.39$, respectively. In the bottom figure, the model predicts two overlapping solutions.

$q < 0$ is the heat flux crossing both thermal walls at vanishing γ. Combining this relation with Eq. (38), we find

$$q^+ = q + \gamma \frac{L}{2}. \tag{39}$$

The objective of our experiments is to measure the apparent conductivity of the suspension

$$k_{\text{eff}} \equiv -qL/(T^+ - T^-). \tag{40}$$

As Fig. 1 illustrates, our strategy identifies three principal paths for the rate $\dot{Q}$ of electrical heat supplied to the central heater of exposed area A_h,

$$\dot{Q} = -A_h q^+ + \frac{(T^+ - T^-)}{R_b} + h_b S_b \left(\frac{T^+ + T^-}{2} - T_\infty \right). \tag{41}$$

In this equation, the first term is the rate of heat transferred to the suspension through the hot plate (path labeled 1 in Fig. 1). The second term represents heat conduction through the ceramic walls of overall thermal resistance R_b (path labeled 2). The third term approximates convective losses from the box as a rate driven by the difference between the intermediate wall temperature $(T^+ + T^-)/2$ and the ambient T_∞, through a constant exchange area S_b at a convection coefficient h_b (path labeled 3). We rearrange Eq. (41) to isolate the dependence of $\dot{Q}$ on T^-,

$$\dot{Q} = -\left(h_b S_b T_\infty + \gamma \frac{A_h L}{2} \right) + T^+ \left(\frac{1}{R_b} + \frac{h_b S_b}{2} + k_{\text{eff}} \frac{A_h}{L} \right) - \Omega T^-, \tag{42}$$

where $\Omega \equiv k_{\text{eff}} A_h/L - h_b S_b/2 + 1/R_b$ is the slope of the linear relation between $\dot{Q}$ and T^-, which we record once a steady-state is achieved. Crucially, this slope is independent of γ and T_∞. Then, by adopting the same protocol for cooling the box in all experiments, we ensure that $(h_b S_b/2 - 1/R_b)$ is a constant. To determine its magnitude, we first run baseline tests with helium. To prevent the latter from escaping the box or from penetrating its air-filled ceramic wall, we coat the inside surface of the cavity with a thin plastic sealant. We then record the slope Ω_{He} of $\dot{Q}$ versus T^-. Because these baseline tests have a low Rayleigh number $Ra = 2gL^3 \rho_g^2 c_g (T^+ - T^-)/(T^+ + T^-)k_g \mu < 800$, they are not affected by free convection [25], and their effective conductivity is that of helium, $k_{\text{He}} = 0.159$ W/m K. Then, for granular suspensions in air, we extract the flux ratio using

$$\frac{\bar{q}}{q_0} = \frac{k_{\text{He}}}{k_{\text{air}}} + (\Omega - \Omega_{\text{He}}) \left(\frac{L}{k_{\text{air}} A_h} \right), \tag{43}$$

where $k_{\text{air}} = 0.0277$ W/m K is the conductivity of air evaluated at a typical temperature of our experiments.

The lumped-parameter data reduction strategy of Eq. (42) assumes that the heat flow is mainly directed along y. We test this assumption with two-dimensional finite-element ANSYS numerical simulations sketched in Fig. 5. In these, ceramic walls and cavity have known conductivities; the heater is a thin rectangle at constant temperature; the cooler and its fins are represented by a thick isothermal rectangle; and convective heat exchanges occur between the external surfaces and the ambient with heat transfer coefficients appropriate to the kind of convection they experience. We run the simulations with values of T^+ and T^- similar to those in experiments and verify that, despite external losses, the electrical energy supplied to the central heater plots as a straight line versus T^-, even in the worst case when the cavity is filled with stagnant air, which has the lowest conductivity we can expect to test, and would thus induce the strongest departure from one-dimensional heat flow from heater to cooler.
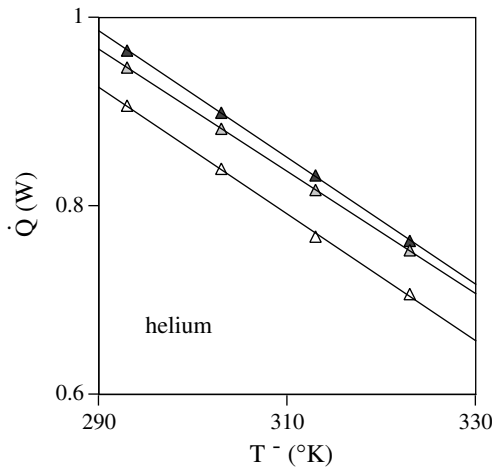
Fig. 6 shows experimental data for evaluating the helium baseline slope. Although the intercept of $\dot{Q}$ versus T^- can vary with changes in ambient conditions, Ω_{He} is remarkably insensitive to those changes. From this graph, we adopt $\Omega_{\text{He}} = 6.6 \times 10^{-3}$ W/K. Fig. 7 is typical raw data for 4 mm acrylic spheres vibrated in air.

Although the Rayleigh number of the helium-filled cavity was too small to portend any free convection in baseline tests, we suspected that experiments with air alone ($Ra \sim 48,000$) could be
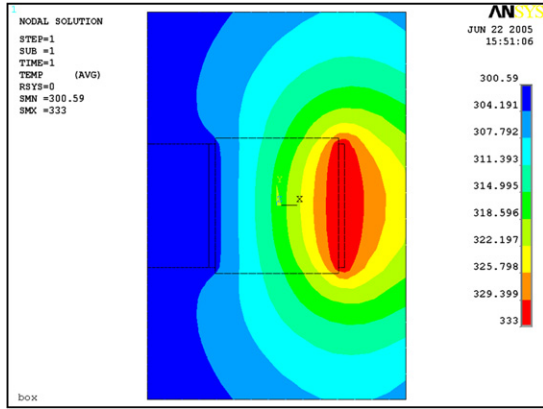
Fig. 5. A typical two-dimensional finite-element ANSYS numerical simulation of heat flow through the box. The square internal cavity has a uniform $k_g = 0.13$ W/m K. The outside is air at 300 K. We estimate free convection coefficients $h_e = 4$ W/m^2 K from available correlations [25] for all external surfaces but the cooler's shown on the left. For the latter, we assume instead that forced convection extracts heat at a coefficient $h_{c1} = 20$ W/m^2 K from cooling fins represented as an isothermal rectangle behind the TEM cooler. On the ceramic (left) surface above and below the fins, we assume an intermediate $h_{c2} = 8$ W/m^2 K.


Fig. 7. Power consumption of the central heater versus cooler temperature for acrylic spheres of 4 mm vibrated in air at, from bottom to top, $a_0 = 0.72, 1.27, 1.69$, and 1.96 mm with $f = 50$ Hz and $\bar{v} = 0.065$. From the least-square fits and Eq. (43), we calculate, respectively, $\bar{q}/q_0 = 4.3, 4.2, 5.6$, and 6.0 from the slopes of these lines. We do not exploit their intercepts, which, according to Eq. (42), depend upon γ and T_∞ as well as k_{eff}.

Fig. 6. Power consumption of the central heater versus cooler temperature to determine the helium baseline slope Ω_{He}. The three runs with different symbols indicate different ambient conditions. Lines are least-squares fits to experimental data.
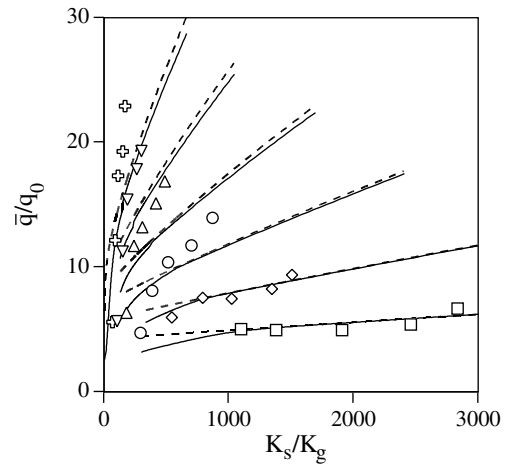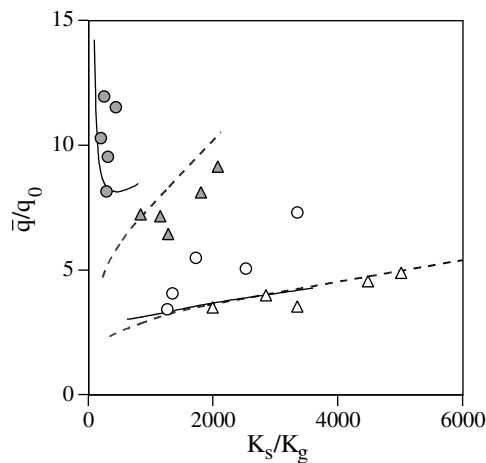

Fig. 8. Variations of $\bar{q}/q_0$ with K_s/K_g and $\bar{v}$ for acrylic spheres with $L/d = Z/d = 12.7$. K_s/K_g is calculated from Eqs. (2) and (5) using $\bar{v}$ and $\overline{\Theta}_{ns}^*$ in Tables 3–6. From bottom to top, squares, diamonds, circles, upward triangles, downward triangles and crosses are data at $\bar{v} = 0.065, 0.13, 0.195, 0.26, 0.325$, and 0.39, respectively. Dashed lines are the corresponding predictions of the thermal theory in Eq. (1), assuming uniform v and Θ in the box. Solid lines are predictions of Eq. (32) combining the thermal theory of Eq. (1) with vertical profiles of v and Θ from the vibration model of Section 2.2. Small kinks in the solid lines near $K_s/K_g = 380, 240$ and 145 for $\bar{v} = 0.26, 0.325$ and 0.39, respectively, are due to jumps from collapsed to agitated solutions of the vibration model.

tainted by such effects. Using Eq. (43) to reduce data similar to Fig. 6, we calculated an apparent conductivity for clean air as much as 21% above k_{air} without vibration, and as high as 70% with vibration. Although this increase is smaller than what is expected of free convection in a cavity of this size and value of Ra [25], confinement by the side walls of normal x likely frustrated the development of free convection of air in the box, and further reassured us that free convection should not affect helium baseline tests. Similarly, the presence of rapidly moving grains should also make free convection irrelevant to agitated suspensions.

3. Results

Tables 3–6 lists all data and model predictions for the flux ratio $\bar{q}/q_0$ versus dimensionless acceleration Γ for acrylic and aluminum spheres. They also include simulation measurements and model predictions of mean dimensionless temperature $\overline{\Theta}^*$, and the corresponding values of K_s/K_g from Eqs. (2) and (5). In these tables, values of $\bar{q}/q_0$ in boldface represent conditions for which the heat

generated by particle collisions is at least 10% of the nominal heat transferred through the hot plate, i.e., $\gamma L/2 > 0.1|q|$. Such conditions are typically observed with relatively dense suspensions of large spheres at high agitation.

As Figs. 8 and 9 illustrate, our thermal theory captures variations of $\bar{q}/q_0$ with K_s/K_g, $\bar{v}$ and L/d in the exchange limit. These figures also indicate that vertical variations of v and Θ can affect $\bar{q}/q_0$ substantially at low agitation. Fig. 10 highlights the role of $\xi_s = k_s/k_g$ and, to a lesser extent, of the Biot number, by comparing $\bar{q}/q_0$ for aluminum and acrylic spheres of the same diameter. Unfortunately, because aluminum spheres dissipate agitation at a greater rate, their suspensions are all partially collapsed near the bottom (see for example Fig. 3, dashed lines), and predictions are more difficult. Curiously, the model suggests that, for aluminum, $\bar{q}/q_0$ can
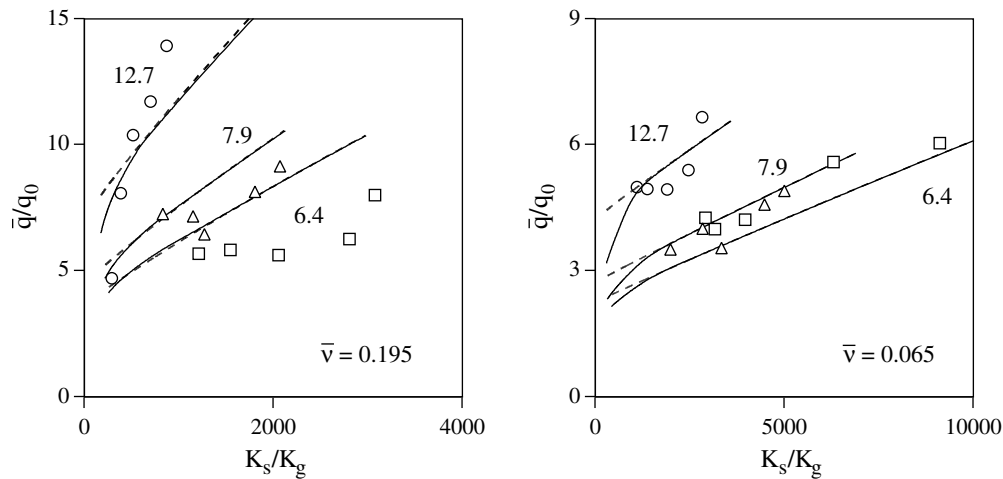
Fig. 9. Variations of $\bar{q}/q_0$ with K_s/K_g for acrylic spheres at $\bar{v} = 0.195$ (left) and $\bar{v} = 0.065$ (right). From bottom to top, squares, triangles and circles are $L/d = Z/d = 6.4$, 7.9, and 12.7, respectively. Lines, see Fig. 8.

Fig. 10. Variations of $\bar{q}/q_0$ with K_s/K_g for acrylic (triangles) and aluminum spheres (circles) for $L/d = Z/d = 7.9$ at $\bar{v} = 0.195$ (filled symbols) and $\bar{v} = 0.065$ (open symbols). Lines represent theoretical predictions of Eq. (32) for aluminum (solid lines) and acrylic spheres (dashed lines).

increase as the suspension tends to small K_s/K_g. This is because the collapsed region experiences greater volume fractions, which raise K_g/k_g considerably due to aluminum's greater values of ξ_s (see Eq. (34)). A complicating issue is that aluminum spheres showed signs of contamination from copper oxide acquired through multiple impacts with thermal walls, thus changing their surface properties in unpredictable ways. Overall, we do not trust our data for aluminum spheres as much as those for acrylic. Nonetheless, the aluminum data marks a transition from the agitated regime of interest to the pure conduction through a static bed of grains, which Vargas and McCarthy explored [3]. In their experiments, because the area of contact between spheres dominates the effective conductivity of the packing, it was crucial to control the applied stresses carefully, a precaution which we could not reliably achieve in our setup.

4. Conclusions

In Part II, we described experiments testing our theoretical predictions for the enhancement of heat flux through thermal walls of vessels containing a gas and agitated spheres in the "exchange limit". Agitation was conferred on the particles in a rectangular box vibrated in the vertical direction. A two-dimensional temperature field was established by surrounding the central measurement heater with a thermal guard, by cooling the opposite wall with thermoelectric modules, and by maintaining both hot and cold thermal walls at distinct steady temperatures. We developed a protocol to infer heat flux from the slope of a graph plotting power supplied to the central heater versus temperature of the cold wall. The protocol kept our results independent of conduction through the ceramic walls of the box, of convection losses from the box, and of heat generated by inelastic granular collisions. However, gravity compelled us to calculate vertical profiles of granular temperature and volume fraction before interpreting the data.

We carried out tests with acrylic and aluminum spheres. Because acrylic spheres had nearly elastic collisions, they yielded more reliable data, and confirmed predictions of the thermal model for variations of heat flux with agitation, solid volume fraction and particle size. On the other hand, because suspensions of relatively inelastic aluminum spheres were more likely to collapse and to develop collision-induced surface contamination, their data were less reliable. Overall, our experiments showed the merits of the thermal model described in Part I, but left open to further research experimental comparisons in the "diffusion limit." To access the latter with macroscopic grains, it is necessary to operate in long-term microgravity, so that a thermal steady-state may be established without collapsing the gas–solid suspension. Colloidal suspensions also reside in the diffusion limit. We will discuss them in Part III.

References

[1] J.S. Patton, R.H. Sabersky, C.E. Brennen, Convective heat transfer to rapidly flowing granular materials, Int. J. Heat Mass Transfer 29 (1986) 1263–1269.
[2] V.V.R. Natarajan, M.L. Hunt, Heat transfer in vertical granular flows, Exp. Heat Transfer 10 (1997) 89–107.
[3] W.L. Vargas, J.J. McCarthy, Heat conduction in granular materials, AIChE J. 47 (2001) 1052–1059.
[4] X. Chen, M. Louge, Heat transfer enhancement in suspensions of agitated solids – Part I: Theory, Int. J. Heat Mass Transfer 51 (2008) 5108–5118.
[5] N.F. Carnahan, K.E. Starling, Equation of state for non-attracting rigid spheres, J. Chem. Phys. 51 (1969) 635–636.
[6] R.E. Meredith, C.W. Tobias, Resistance to potential flow through a cubical array of spheres, J. Appl. Phys. 31 (1960) 1270–1273.

[7] D. Henderson, F.F. Abraham, J.A. Barker, The Onrstein–Zernike equation for a fluid in contact with a surface, Mol. Phys. 31 (1976) 1291–1293; D. Henderson, F.F. Abraham, J.A. Barker, The Onrstein–Zernike equation for a fluid in contact with a surface, Mol. Phys. 100 (2002) 129–132.

[8] R. Verberg, D.L. Koch, Rheology of particle suspension with low to moderate fluid inertia at finite particle inertia, Phys. Fluids 18 (2006) 083303.

[9] S. Whitaker, Forced convection heat transfer correlations for flow in pipes, past flat plates, single cylinders, single spheres, and for flow in packed beds and tube bundles, AIChE J. 18 (1972) 361–371.

[10] X. Chen, Thermal transport in suspensions of gases and agitated solids, Ph.D. Thesis, Cornell University, Ithaca, NY, 2006.

[11] S.F. Foerster, M.Y. Louge, H. Chang, K. Allia, Measurements of the collision properties of small spheres, Phys. Fluids 6 (1994) 1108–1115.

[12] A. Lorenz, C. Tuozzolo, M.Y. Louge, Measurements of impact properties of small, nearly spherical particles, Exp. Mech. 37 (1997) 292–298.

[13] R.D. Wildman, J.T. Jenkins, P.E. Krouskop, J. Talbot, A comparison of the predictions of a simple kinetic theory with experimental and numerical results for a vibrated granular bed consisting of nearly elastic particles of two sizes, Phys. Fluids 18 (2006) 073301.

[14] H. Viswanathan, R.D. Wildman, J.M. Huntley, T.W. Martin, Comparison of kinetic theory predictions with experimental for a vibrated three-dimensional granular bed, Phys. Fluids 18 (2006) 113302.

[15] V. Kumaran, Temperature of a granular material "fluidized" by external vibrations, Phys. Rev. E 57 (1998) 5660–5664.

[16] J. Bougie, S.J. Moon, J.B. Swift, H.L. Swinney, Shocks in vertically oscillated granular layers, Phys. Rev. E 66 (2002) 051301.

[17] M.A. Hopkins, M.Y. Louge, Inelastic microstructure in rapid granular flows of smooth disks, Phys. Fluids A 3 (1991) 47–57.

[18] E. Falcon, R. Wunenburger, P. Evesque, S. Fauve, C. Chabot, Y. Garrabos, D. Beysens, Cluster formation in a granular medium fluidized by vibrations in low gravity, Phys. Rev. Lett. 83 (1999) 440–443.

[19] A.S. Sangani, G. Mo, H.-K. Tsao, D.L. Koch, Simple shear flows of dense gas–solid suspensions at finite Stokes numbers, J. Fluid Mech. 313 (1996) 309–341.

[20] D.L. Koch, A.S. Sangani, Particle pressure and marginal stability limits for a homogeneous monodisperse gas fluidized bed: kinetic theory and numerical simulations, J. Fluid Mech. 400 (1999) 229–263.

[21] J.T. Jenkins, M.W. Richman, Grad's 13-moment system for a dense gas of inelastic spheres, Arch. Ration. Mech. Anal. 87 (1985) 355–377.

[22] M.W. Richman, Boundary conditions for granular flows at randomly fluctuating bumpy boundaries, Mech. Mater. 16 (1993) 211–218.

[23] M.Y. Louge, Computer simulations of rapid granular flows of spheres interacting with a flat, frictional boundary, Phys. Fluids 6 (1994) 2253–2269.

[24] S. Torquato, Nearest-neighbor statistics for packings of hard spheres and disks, Phys. Rev. E 51 (1995) 3170–3182.

[25] F.P. Incropera, D.P. Dewitt, Fundamentals of Heat and Mass Transfer, fifth ed., John Wiley, NY, 2002.